addenda and errata

ANKAphase: software for single-distance phase retrieval from inline X-ray phase-contrast radiographs. Erratum

T. Weitkamp,[a]* **D. Haas,**[b,c] **D. Wegrzynek**[d]‡ **and A. Rack**[e]*

[a]Synchrotron Soleil, Gif-sur-Yvette, France, [b]Institute for Synchrotron Radiation/ANKA Light Source, KIT, Karlsruhe, Germany, [c]Hochschule Darmstadt, Darmstadt, Germany, [d]International Atomic Energy Agency, Seibersdorf, Austria, and [e]European Synchrotron Radiation Facility, Grenoble, France.
E-mail: weitkamp@synchrotron-soleil.fr, arack@snafu.de

An equation in the paper by Weitkamp *et al.* [(2011), *J. Synchrotron Rad.* **18**, 617–629] is corrected.

There was a mistake in equation (6) in the paper by Weitkamp *et al.* (2011). The equation should read

$$\varphi(x, y) = \frac{\delta}{2\beta} \ln\left(\mathcal{F}^{-1}\left\{ \frac{\mathcal{F}\left[I(x,y)/I_0(x,y)\right]}{1 + [\lambda z \delta/(4\pi\beta)]\,(u^2 + v^2)} \right\} \right). \tag{6}$$

References

Weitkamp, T., Haas, D., Wegrzynek, D. & Rack, A. (2011). *J. Synchrotron Rad.* **18**, 617–629.

‡ Present address: University of Science and Technology, Kraków, Poland.

doi:10.1107/S0909049512044871

ANKAphase: software for single-distance phase retrieval from inline X-ray phase-contrast radiographs

T. Weitkamp,[a]* D. Haas,[b,c] D. Wegrzynek[d]‡ and A. Rack[e]*

[a]Synchrotron Soleil, Gif-sur-Yvette, France, [b]Institute for Synchrotron Radiation/ANKA Light Source, KIT, Karlsruhe, Germany, [c]Hochschule Darmstadt, Darmstadt, Germany, [d]International Atomic Energy Agency, Seibersdorf, Austria, and [e]European Synchrotron Radiation Facility, Grenoble, France. E-mail: weitkamp@synchrotron-soleil.fr, arack@snafu.de

A computer program named *ANKAphase* is presented that processes X-ray inline phase-contrast radiographs by reconstructing the projected thickness of the object(s) imaged. The program uses a single-distance non-iterative phase-retrieval algorithm described by David Paganin *et al.* [(2002), *J. Microsc.* **206**, 33–40]. Allowing for non-negligible absorption in the sample, this method is strictly valid only for monochromatic illumination and single-material objects but tolerates deviations from these conditions, especially polychromaticity. *ANKAphase* is designed to be applied to tomography data (although it does not perform tomographic reconstruction itself). It can process series of images and perform flat-field and dark-field correction. Written in Java, *ANKAphase* has an intuitive graphical user interface and can be run either as a stand-alone application or as a plugin to *ImageJ*, a widely used scientific image-processing program. A description of *ANKAphase* is given and example applications are shown.

1. Introduction

Hard X-ray imaging with high spatial resolution is an established analytical tool for investigating specimens in two or three dimensions and in a widely non-destructive manner. Its capabilities can be significantly extended when synchrotron light sources are employed, as higher resolution in space and time as well as sophisticated contrast modes become accessible. For a brief introduction to the techniques the reader is referred to the literature (*e.g.* Graeff & Engelke, 1991; Stevenson *et al.*, 2003; Banhart, 2008; Stock, 2008; McMorrow & Als-Nielsen, 2011).

A simple but powerful approach to access higher imaging sensitivity when using synchrotron light sources is a technique known as X-ray inline phase contrast or propagation-based phase contrast: by leaving an appropriate drift space between the sample and the imaging detector (Fig. 1), interfaces within the probed specimen can be visualized. If the X-ray wavefront has a sufficient degree of transverse coherence, Fresnel diffraction on microscale structures will lead to interference fringes that enhance edges and interfaces of the sample in the recorded radiogaph (Snigirev *et al.*, 1995; Cloetens *et al.*, 1996;

‡ Present address: University of Science and Technology, Kraków, Poland.

Nugent *et al.*, 1996; Wilkins *et al.*, 1996). Compared with the conventional absorption contrast, X-ray inline phase contrast allows studying objects with either negligible absorption or multi-constituent samples in which the different components show too similar absorption to be discriminated.

In projection radiographs, for near-transparent structures whose smallest resolved feature size d fulfils the condition $d \gg (\lambda z)^{1/2}$ (where λ is the X-ray wavelength and z the distance between the object and the detector plane; see Fig. 1), the phase-contrast signal can be approximated (Bremmer, 1952) as the Laplacian of the wavefront phase profile, $\nabla^2_{xy}\varphi(x, y)$ (where x and y are the Cartesian coordinates in the image and/or object plane). Tomographic reconstruction without phase retrieval yields the three-dimensional distribution of the Laplacian of the decrement of refractive index, $\nabla^2_{x'y'z'}\delta(x', y', z')$ (where x', y', z' are the Cartesian coordinates in the image and/or object plane) (Weitkamp, 2002). While this information is often useful for visual inspection of the data by a human beholder, any further quantitative analysis that requires segmentation of the tomography volume data is not easily possible using the plain phase-contrast data. This is because the gray levels within the different materials regions are not necessarily different; they are just varying at the interfaces. In other words, there is no direct correlation
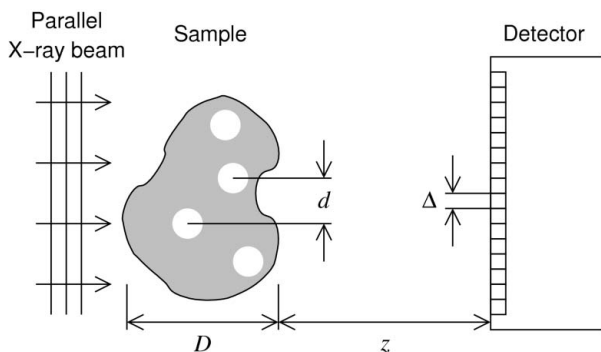
Figure 1
Schematic representation of a parallel-beam inline phase-contrast radiography or tomography set-up for which the *ANKAphase* computer program is designed. A near-parallel X-ray beam passes through a sample with hidden internal microstructure. The smallest resolved structures have a characteristic size d. Radiographs are recorded on a detector with pixels of size Δ, placed at a single fixed distance z from the sample. In real set-ups the sample diameter is much smaller than the propagation distance, *i.e.* $D \ll z$.

between the gray level of a voxel and the material or density corresponding to this voxel. Without the use of phase retrieval, complex routines need to be developed and applied to make segmentation possible (Antoine *et al.*, 2002; Socha & De Carlo, 2008), or the segmentation attempts will only label the interfaces (Thurner *et al.*, 2003; Rabaglino *et al.*, 2003). In particular, properly segmented data are needed for such three-dimensional image-analysis tasks as the derivation of statistical information or to approach sophisticated problems, *e.g.* spatial correlations between different constituents within the investigated specimens (Zabler *et al.*, 2007; Manke *et al.*, 2007; Stiller *et al.*, 2009; Ohser & Schladitz, 2009; Rack *et al.*, 2009a; Brun *et al.*, 2010).

If, however, the transmission radiographs are sent through a phase-retrieval process, and the tomographic reconstruction is performed on the phase projection maps obtained by phase retrieval, the tomograms will exhibit 'area contrast' rather than edge-enhancing contrast. This means that the value of each pixel in a reconstructed slice (or voxel in a reconstructed volume) is directly related to the material of the object at this position. The data can therefore be much easier segmented. In particular, software tools originally developed for the segmentation of absorption-contrast data can be used, taking advantage of the higher sensitivity of phase contrast. Phase retrieval is thus crucial whenever tomography data obtained in propagation-based phase-contrast imaging need to be segmented.

A variety of phase-retrieval methods for X-ray inline phase-contrast data have been developed since the mid-1990s. Some of the proposed methods are iterative (Kohn, 1997; Schelokov *et al.*, 2002; Meng *et al.*, 2007), but most use analytical approaches. These non-iterative methods differ in the amount of raw data needed (in particular, many methods require images taken at different distances z), restrictions on sample composition and/or X-ray optical properties of the sample, properties of the X-ray beam, and quality of the reconstruction, in particular, accuracy of the reconstructed phase values

and spatial resolution of the results. (For published examples, see Maleki & Devaney, 1994; Nugent *et al.*, 1996; Cloetens *et al.*, 1999; Gureyev *et al.*, 1999, 2002; Schelokov *et al.*, 2002; Bronnikov, 2002; Paganin *et al.*, 2002; Wu *et al.*, 2005; Groso *et al.*, 2006a,b; Langer *et al.*, 2008; Wu & Yan, 2009; Moosmann *et al.*, 2010.)

For the software tool presented here, a single-distance phase-retrieval method developed by Paganin *et al.* (2002) was chosen. This particular algorithm was selected among other methods that retrieve the phase from radiographs taken at a single distance because unlike many of these methods it does not require the sample to show only negligible absorption. Instead, it assumes that the sample is made of a single material. This means that retrieval of the wavefront phase $\varphi(x, y)$ at the sample exit plane is equivalent to retrieval of the projected sample thickness $t(x, y)$, as these two quantities are related to each other by

$$\varphi(x, y) = -\frac{2\pi\delta}{\lambda} t(x, y). \tag{1}$$

The algorithm is derived for monochromatic illumination. Further below we shall demonstrate that, in practice, Paganin's approach shows substantial tolerance to violation of these two conditions, in accordance with theoretical predictions and experimental results (Myers *et al.*, 2007). The method has already demonstrated its high potential for specimens from diverse scientific fields (Peele *et al.*, 2005; Wang *et al.*, 2006; Irvine *et al.*, 2008; Xu *et al.*, 2010; Mayo *et al.*, 2010). In several studies of this kind the software presented here was used (Ohser *et al.*, 2009; Denecke *et al.*, 2011; Mochales *et al.*, 2011).

The computer program we present is a simple but robust tool which runs independent of hardware platform and operating system and has an intuitive graphical user interface. It is our hope that this will make phase-sensitive imaging techniques, including phase reconstruction, available to a wider range of synchrotron users. This is of particular interest for scientific fields where excellent volume renderings are required, for example in biology (Westneat *et al.*, 2003, 2008; Socha *et al.*, 2007). Furthermore, quantitative volume image analysis will become feasible for tomographic images acquired *via* edge-enhanced projections without extensive data pre-processing (Antoine *et al.*, 2002; Martín-Herrero & Germain, 2007). Data taken in the past without any original intent of phase retrieval may be re-visited for phase reconstruction. Finally, since X-ray inline phase contrast is accessible under moderate coherence conditions and even with polychromatic radiation, semi-quantitative phase-sensitive imaging becomes possible at a broader range of synchrotron light sources (Peele *et al.*, 2005; Cholewa *et al.*, 2007; Kohn *et al.*, 2007; Rack *et al.*, 2010), and even with specific laboratory sources (Tuohimaa *et al.*, 2007; Boone *et al.*, 2009).

2. Theory

In this section we give a short synopsis of the algorithm used by *ANKAphase* and first published by Paganin *et al.* (2002).

We also outline technical aspects related to the implementation.

2.1. The phase reconstruction algorithm

Although in practice applicable over a wide parameter range, and in particular for polychromatic radiation, partially coherent illumination and objects with density variations, the algorithm is originally derived based on the following assumptions:

(i) The object imaged consists of a single homogeneous material.

(ii) The incident wave is monochromatic.

(iii) The incident wave is a plane wave or only mildly curved.

(iv) The distance z between the object and the detector plane fulfils the near-field condition, *i.e.*

$$z \ll d^2/\lambda, \tag{2}$$

where d is the characteristic size of the smallest discernible features in the object, and λ is the X-ray wavelength. Fig. 1 schematically shows a set-up of this kind.

If these conditions are met, the intensity distribution $I(x, y)$ measured at a single known distance z between the object and the detector plane can be used to retrieve the projected thickness $t(x, y)$ of the object (or, which is equivalent, the projected phase shift of the X-ray wavefront) using the relation

$$t(x, y) = -\frac{1}{\mu} \ln\left(\mathcal{F}^{-1}\left\{ \frac{\mathcal{F}[I(x, y)/I_0(x, y)]}{1 + z\delta\mu^{-1}(u^2 + v^2)} \right\} \right). \tag{3}$$

Here, x and y are the Cartesian coordinates in the image and/or object plane, μ is the linear attenuation coefficient of the object material, $\mathcal{F}$ and $\mathcal{F}^{-1}$ are, respectively, the forward and backward Fourier transform operators, $I(x, y)$ is the intensity distribution in the phase-contrast radiograph, $I_0(x, y)$ is the incident intensity without the object at the position of the detector, δ is the decrement from unity of the X-ray refractive index of the object material, u, v are the Fourier conjugate coordinates of x and y, and z is the object–detector distance. The quantities δ and μ are related to the complex-valued X-ray refractive index n by

$$n = 1 - \delta + i\beta, \tag{4}$$

$$\mu = 4\pi\beta/\lambda, \tag{5}$$

where i is the imaginary unit number as defined by $i^2 = -1$. Both β and δ are dimensionless real numbers.

In practice, the near-field condition (2) means that, in order to achieve a desired spatial resolution d, the propagation distance z should be substantially shorter than d^2/λ. Since the spatial resolution cannot be better than twice the detector pixel size Δ, we can define a critical distance $z_c = (2\Delta)^2/\lambda$. A choice of z that makes full use of the detector resolution will have to be shorter than z_c to fulfil the near-field condition. (If the actual optical resolution d_{res} of the detector system is known, 2Δ can be replaced by d_{res} in the definition of z_c.) Fig. 2 illustrates typical values and may help experimentalists
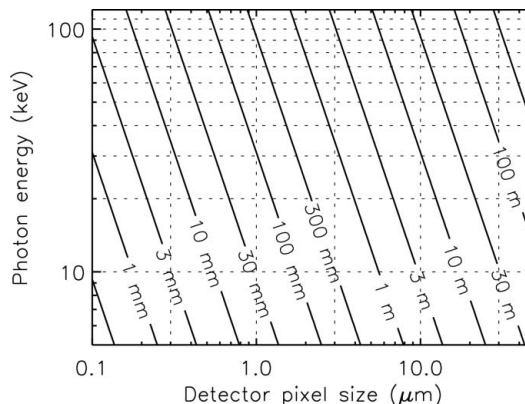

Figure 2
Contour plot of the critical propagation distance $z_c = (2\Delta)^2/\lambda$, for pixel sizes Δ ranging between 0.1 and 50 µm and photon energies from 5 to 120 keV. The actual distance z between sample and detector in a detector should be chosen well below z_c to fulfil the near-field condition (2) even for the smallest features that the detector can resolve.

in choosing a suitable sample–detector distance for their measurements. The maximum reasonable value of z can be additionally reduced by limited transverse coherence of the X-ray beam at the sample position.

If the object under study consists of a material that is not homogeneous but in which the fraction β/δ is constant, the algorithm remains valid. Particular cases in which this relaxed condition is met are (i) objects with homogeneous elemental composition but varying density and (ii) objects in which absorption is negligibly weak, *i.e.* β is very close to zero.

In these cases it is useful to consider the reconstructed phase map $\varphi(x, y)$ as the quantity of interest, rather than the projected thickness $t(x, y)$, because the latter is not meaningful if the material density varies. Using equations (1) and (5), the reconstruction formula (3) can be rewritten as

$$\varphi(x, y) = \frac{1}{2} \ln\left(\mathcal{F}^{-1}\left\{ \frac{\mathcal{F}[I(x, y)/I_0(x, y)]}{\beta/\delta + [\lambda z/(4\pi)](u^2 + v^2)} \right\} \right). \tag{6}$$

It is obvious from (6) that the reconstructed phase map $\varphi(x, y)$ will only depend on the ratio β/δ but not on the absolute estimated value of each of these two quantities. An important implication of this is that, if the mass density of a sample material is not exactly known, the reconstructed phase maps will still be correct as long as the chemical composition is known. In this case, which is frequent for biological materials, the reconstructed thickness maps $t(x, y)$ will differ from the true thicknesses only by a constant factor that is equivalent to the relative error in density. The reconstructed phase tomograms will also only differ by this constant factor from the true value of the reconstructed quantity.

While *ANKAphase* reconstructs thickness values as obtained through equation (3), in millimeter units, these can be easily interpreted as phase values by applying the relationship expressed in equation (1) in cases where this is deemed more appropriate.

research papers

2.2. Flat-field and dark-field correction

In a real X-ray imaging system the background signal (*i.e.* the signal recorded if no object is in the beam) is generally not uniform. This can be due to inhomogeneities in the X-ray beam intensity distribution or to non-uniform detector response (caused, for example, by vignetting or varying pixel sensitivities), or both. It is therefore generally necessary to normalize each radiograph by an image of the beam without the object. This is called a flat-field correction. Also, in each image recorded with the detector, the offset signal recorded when no photons hit the detector (dark signal) should be subtracted from the image before further processing (dark-field correction). The corrected images are

$$I_c(x, y) = \frac{I(x, y)}{I_0(x, y)} = \frac{S_o(x, y) - S_d(x, y)}{S_f(x, y) - S_d(x, y)}, \qquad (7)$$

where $S_o(x, y)$ is the image signal measured with the object in the beam, $S_d(x, y)$ is the dark signal, and $S_f(x, y)$ the flat signal (*i.e.* the image with the sample removed). In order to keep the increase of statistical noise introduced by the correction to a minimum, it is preferable to take a series of flat-field and dark images and average these before using them for correcting the object images. *ANKAphase* can perform flat-field and dark-image correction of the radiographs. It can process series of flat-field images, as well as series of dark images by calculating, for every pixel, the average gray value for that pixel, where the averaging is performed over all images in the series (but separately for each pixel). In doing this, *ANKAphase* uses median averaging (rather than the arithmetic mean).

2.3. Boundary treatment

To avoid cross-talk between opposed ends of the images the recorded projections have to be padded to a larger size before applying the phase-retrieval algorithm. Without padding, cross-talk occurs because the convolution of the projection data with a phase-reconstruction kernel is carried out in Fourier space, so that the convolution is periodic (Press *et al.*, 2007). Further padding is required because the fast Fourier transform (FFT) routine used requires the number of pixels in each dimension to be a power of two.

The images are therefore padded in a two-stage approach. First, the original image with dimensions (n_x, n_y) is extended by a margin on all four sides (top, bottom, left, right) of width

$$n_{\mathrm{margin}} = \lceil 3\lambda z/\Delta^2 \rceil. \qquad (8)$$

Here, Δ is the effective pixel size of the detector, z the propagation distance and λ the X-ray wavelength. The brackets $\lceil \ldots \rceil$ denote the ceiling operation, which yields the smallest integer number that is equal to or greater than the argument.

In a second step, the image with the new dimensions (n'_x, n'_y), where $n'_i = n_i + 2n_{\mathrm{margin}}$, is further padded so that finally both dimensions are powers of two. Each pixel in the padded area is filled with the value of the nearest pixel in the original image. The final dimensions of the image are thus $n''_i = \exp\{(\ln 2)\lceil \log_2 n'_i \rceil\}$.

Equation (8) is based on the fact that a point-like feature located near the border of the input image will create a diffraction pattern consisting of a series of concentric bright and dark rings. Similar to a zone plate, the width of the outer rings decreases with their distance to the center of the pattern. Using a detector with a given pixel size Δ, the details of the diffraction pattern can no longer be resolved if adjacent bright fringes are spaced by less than the size of a pixel. The additional factor of three excludes remaining aliasing effects. A detailed derivation of equation (8) is given in Appendix *A*.

3. Implementation

ANKAphase is written in Java (Java Consortium, 2010). It can be run as a plugin to the widely used scientific image-processing program *ImageJ* (National Institutes of Health, 2010*b*) or as a stand-alone application. In the latter case *ImageJ* does not need to be running or even installed on the user's computer.

The use of Java as the programming language ensures that the executable program file in the distribution will run on most or all hardware and software platforms for which the Java Runtime Environment is available.

On computers with multiple central processing units (CPUs) or with a CPU with multiple cores, images are processed using multi-threading, which speeds calculations up by parallelizing certain tasks.

The graphical user interface is based on the Java packet *Swing*, again to ensure platform independence. All image-processing routines as well as input and output functions are based on the *ImageJ* library *ij.jar* (National Institutes of Health, 2010*b*). All calculations are performed in double-precision floating-point arithmetic (8 bytes per pixel). The output files contain, depending on the user's choice, integer data of variable bit depth or single-precision float data. The basic concept of the *ANKAphase* software is displayed as a flow process chart in Fig. 3.

4. User interface

A screenshot of *ANKAphase* running as an *ImageJ* plugin under Microsoft Windows XP is shown in Fig. 4. The control elements are identical on other platforms and operating systems. All parameters are accessible in a single control window. Parameter names were chosen according to conventions in use at imaging stations of synchrotron light sources. Therefore, most synchrotron users should be able to handle *ANKAphase* with only minor training effort.

ANKAphase identifies the input image files it will process by the directory in which these files are located. For a given set of images taken under the same experimental conditions and with the same image dimensions for all frames it expects all the projection radiographs to be in one directory, while the series of dark images to be averaged for the dark-field correction are supposed to be in another directory.

For the flat-field images, *ANKAphase* foresees two directories: one in which flat images taken before the acquisition of
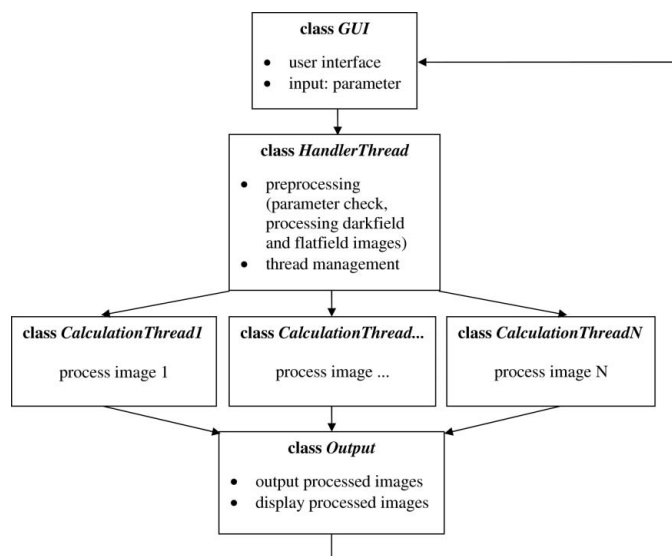
Figure 3
Flow process chart showing the basic design of the *ANKAphase* software as realised in Java.

the projections are stored, and another in which flats taken after the acquisition of the projections are stored. If two blocks of flat-field images obtained in this manner are available, the default behavior of *ANKAphase* is to correct the first half of the projection images using the first set of flat-field images, and the second half of the projections will be corrected using the second set of flat-field images. Interpolation between the two flat-image sets is available as a check-box option.

It is the user's responsibility to ensure that the dimensions and data type of all image files in the input directories are the same. Leaving other files in the corresponding directory will prevent *ANKAphase* from starting to work.

A detailed view of the graphical user interface of *ANKAphase* is shown in Fig. 5. The paths to the files containing the raw data can be entered directly or chosen *via* the file selection dialog of the operating system. Optional functionality can be turned on and off through check boxes. In this way *ANKAphase* offers flexibility and can, for example, even be used to perform only flat-field correction.

ANKAphase recognizes the following file formats, by their file-name extension: TIFF (8-bit unsigned integer, 16-bit unsigned integer and 32-bit single-precision float format), JPEG (8-bit unsigned integer), PNG (8-bit unsigned integer), BMP (8-bit unsigned integer) and the ESRF-specific data format EDF (32-bit single-precision float format) (ESRF, 2010). *ANKAphase* preferably writes output files containing the results in single-precision float format. However, if desired by the user, the results can also be written out in integer-type data formats. If a file format with an integer data type is selected, the corresponding parameters for the data reduction (re-scaling and cropping of saturated values) can be entered manually or determined automatically by *ANKAphase via* the individual minimum and maximum values for each calculated image or the first projection image only.

A standard procedure for processing a set of projections with *ANKAphase* consists of entering the required paths as well as the experimental parameters and activating the flat-field and the phase-retrieval option.

Among the experimental parameters to be specified by the user, the decrement of X-ray refractive index δ and the absorption coefficient β are often the most difficult to obtain
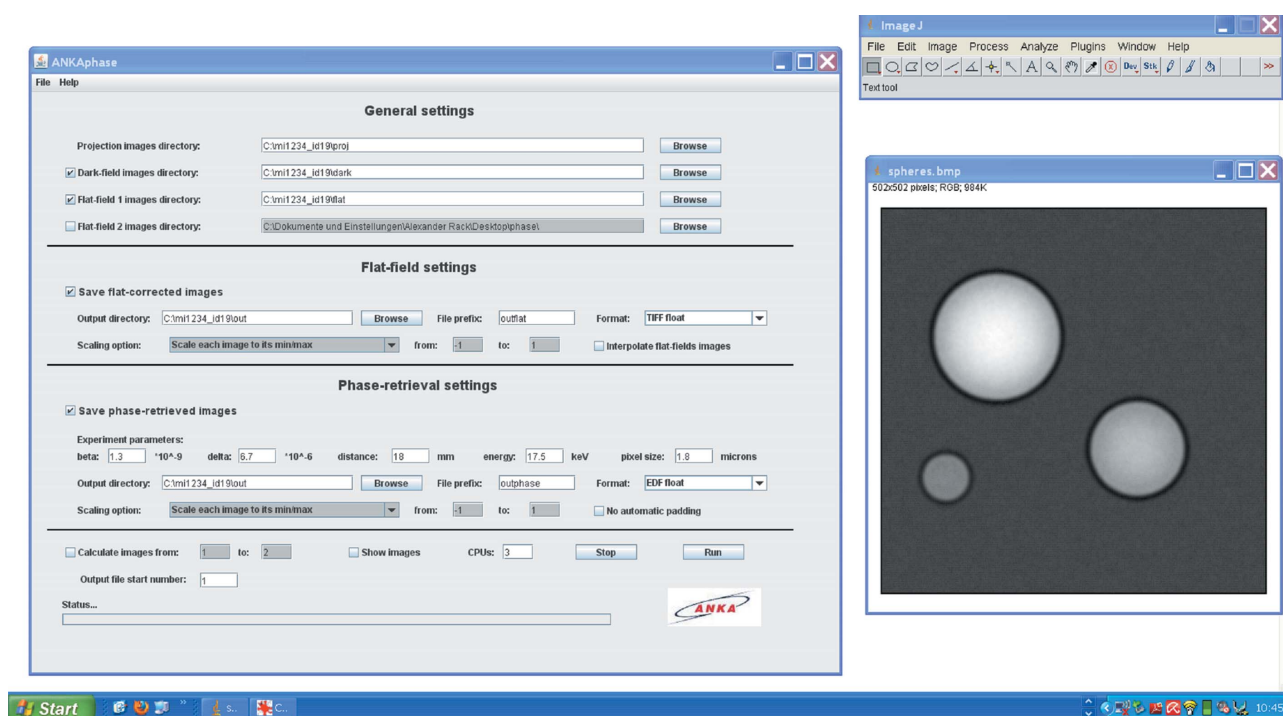

Figure 4
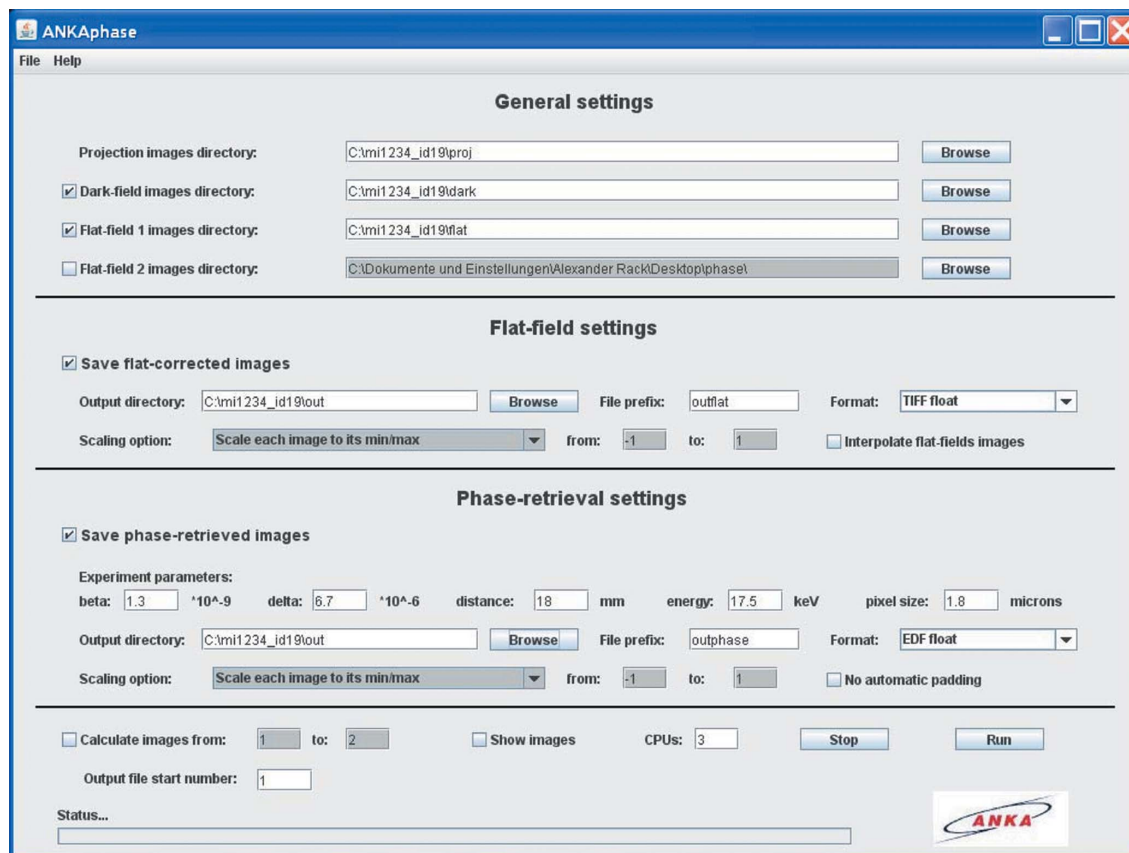Screenshot of *ANKAphase* operated as *ImageJ* plugin under Microsoft Windows XP.

Figure 5
The graphical user interface of *ANKAphase*. All parameters can be directly accessed through a single control window.

because they require some knowledge, at least approximate, about the sample composition, and access to tabulated values. While *ANKAphase* itself does not feature any look-up of X-ray optical properties, tools to calculate δ and β from the stoichiometry and the density of the sample material, or from lists of compound materials, are available as online Web applications (Center for X-ray Optics, 2010; Kuznetsov, undated) or for download. Among these programs the *XOP* software suite (Sanchez del Rio & Dejus, 1998; ESRF, 2009) gives access to a variety of databases for different ranges of photon energies and for a large number of mixtures and compound materials including polymers and biological tissues such as bone, lung or muscle. The tables containing the composition of these compounds can also be directly consulted on the World Wide Web (National Institute of Standards and Technology, 2004).

When starting to work on a data set with *ANKAphase*, it is recommended to calculate, as a first step, only one phase map together with the corresponding flat-field-corrected projection. If the parameters chosen are appropriate, *ANKAphase* will calculate from the flat-field-corrected fringe image a phase map which should be almost void of fringes (see Fig. 6). Users should keep in mind that the algorithm is suited for quasi-homogeneous objects only, *i.e.* for objects in which the ratio of δ and β is rather constant and only the density changes. Phase retrieval of an image that shows, for example, an object made of metal and one made of polymer will yield a phase map

that is not only quantitatively incorrect but will also show remaining fringes or blurred edges around structures for which the assumed value of δ/β is not correct (Beltran *et al.*, 2010).

Once the parameters are set, the full set of projection images can be processed. The number of CPUs used in parallel can be selected by the user. Memory consumption has to be kept in mind (*ANKAphase* will stop with an error message when it cannot allocate enough memory).

A technical remark on dealing with the required file-name and directory structure: frequently, tomographic scans are saved as file series with a fixed filename prefix combined with continuous numbering that includes flat and dark images. It may be undesirable to move these files physically into different directories as would be required by *ANKAphase*. On Unix-like operating systems a simple workaround is to create the folders needed for *ANKAphase* and to fill them with symbolic links pointing towards the corresponding files.

In cases where flat-field images have been taken not only at the beginning and the end of a scan but in between as well, series of folders have to be used, and processing must be launched individually for each lot of projection images between two adjacent flat-field blocks. For such cases, *ANKAphase* has an optional parameter named 'Output file start number' that allows users to create continuously numbered files containing the phase maps.

Once processing is launched, a text-format parameter file containing the settings of the current run will be stored in the output folder. It can be used as an electronic log of the processing and/or to later re-load and apply the same parameters.

Further technical details can be found in Appendix *B* and in the *ANKAphase User Guide* included in the software distribution.

5. Examples

In this section selected examples of phase-retrieval applications based on the use of *ANKAphase* are shown. While they cover only a small area of the diverse scientific fields where phase-sensitive X-ray imaging is beneficial, the examples underline the strength of the algorithm: it can be applied on arbitrarily absorbing samples, in a quantitative manner as well as on projections acquired using polychromatic radiation.

5.1. Quantitative phase retrieval: verification

In case all of the conditions concerning illumination and sample as listed in §2.1 are fulfilled, equation (3) will yield the projected thickness $t(x, y)$ of the imaged objects (equivalent to the projected phase shift of the X-ray wavefront). In order to verify the implementation of *ANKAphase*, a glass capillary was chosen as a simple arbitrarily absorbing specimen and imaged with monochromatic X-rays.

In Fig. 6 (top) a flat- and dark-corrected radiograph of this object is shown, obtained with the micro-imaging set-up at beamline ID22 of the ESRF (Weitkamp *et al.*, 1999). 17 keV radiation from a Si(111) double-crystal monochromator (DCM) was used; the relative spectral bandwidth of the radiation from the DCM is of the order of $\Delta E/E \simeq 10^{-4}$.

For this and all of the following examples, high-resolution indirect X-ray detectors were used. These are lens-coupled systems with a scintillator screen and a digital image sensor based on a charge-coupled device (CCD). The scintillator converts the X-ray intensity distribution to a visible-light image; the lens system magnifies this image and projects it onto the CCD. This scheme was developed during the 1990s (Bonse & Busch, 1996; Koch *et al.*, 1998), shortly after scientific-grade CCDs had become affordable. Today, such optical systems can be bought from commercial suppliers, *e.g.* Optique Peter, Lyon, France, although high-resolution scintillator screens of high quality remain difficult to obtain and often still require additional dedicated development by the synchrotron laboratories (Martin & Koch, 2006; Martin *et al.*, 2009; Douissard *et al.*, 2010).

For the example in this section, the scintillator was a 6.2 μm-thick GGG:Eu (Eu-doped $Gd_3Ga_5O_{12}$) single crystal grown on top of an undoped GGG substrate. It was positioned 15 mm away from the sample. The light from the scintillator was projected onto the chip of a FReLoN 2000 camera by a microscope optic consisting of a $10\times$ objective with a numerical aperture (NA) of 0.4 and a $2\times$ eyepiece (Martin & Koch, 2006; Labiche *et al.*, 2007). Since the CCD pixels have a
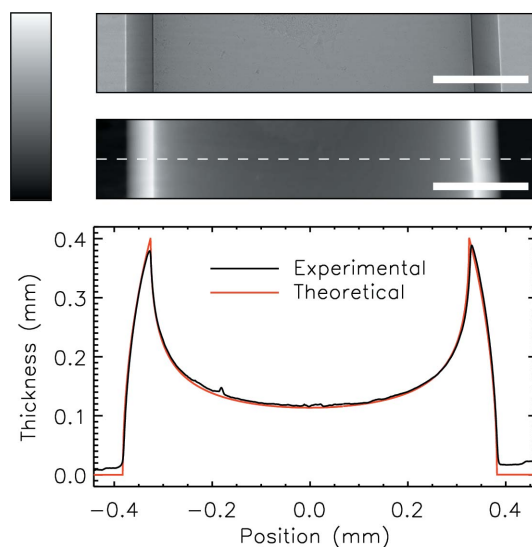

Figure 6
Quantitative phase retrieval. Top: projection radiograph of a glass capillary, taken with monochromatic X-rays of 17 keV and at a sample–detector distance of 15 mm. The image has been corrected for dark signal and flat-field-normalized. The grayscale image shows the transmission signal I/I_0, scaled between 0.4 (black) and 1.3 (white). The length of the scale bar is 200 μm. Center: image after phase reconstruction using Paganin's formula. The gray levels represent reconstructed values of the projected glass thickness between 0 (black) and 0.4 mm (white). Bottom: section profile line through the reconstructed projection image (at the position indicated by the dashed white line in the radiograph), and expected profile (red) for a capillary of outer diameter 0.765 mm and wall thickness 57 μm. The X-ray optical properties used in the reconstruction were those from the DABAX database (Sanchez del Rio & Dejus, 1998) for SiO_2 with a density of 2.4 g cm^{-3} at 17 keV: $\delta = 1.73 \times 10^{-6}$, $\beta = 5.01 \times 10^{-9}$. Data taken at ESRF-ID22 with an effective pixel size of 0.7 μm.

size of 14 μm, the effective pixel size with which the image was sampled was 0.7 μm.

The spatial resolution of this detector configuration was around 2 μm. It was measured using an X-ray test pattern model X-500-200-30 (Xradia, Pleasanton, CA, USA). Test patterns of the same type were also used for the resolution measurements related to the results in the following sections.

For the phase retrieval, values of β and δ corresponding to SiO_2 (2.4 g cm^{-3}) were used, obtained from the DABAX database (Sanchez del Rio & Dejus, 1998). The calculated phase map is shown in Fig. 6 (middle). With the inner and outer capillary radii known, the projected thickness of the object can be calculated as well. A combined plot showing the retrieved projected thickness profile and the theoretical one are shown in Fig. 6 (bottom). The agreement between experimental data and theory is remarkable.

5.2. Materials research

The example shown in this section has a twofold function as it stands both for materials research and for an object for which little *a priori* information on its exact constituents was available: a sample of recycled paper (kindly provided by the Papiertechnische Stiftung PTS, Munich, Germany). The microstructure of paper determines important mechanical

properties such as its tensile strength or filtration properties. Therefore, paper microstructure has been studied for a long time, yet mainly based on two-dimensional imaging techniques such as scanning electron microscopy. For the study shown here, an X-ray microtomography data set was acquired in a 'local tomography' geometry (with the sample size exceeding the field of view of the detector), again using the microtomography stage at ID22 of the ESRF with monochromatic radiation from the crystal monochromator of this beamline. The X-ray photon energy for this study was 13 keV. The pixel size of the detector was 0.35 μm, obtained through a 20× objective (NA 0.7) and a 2× eyepiece that projected the image from a 3.5 μm-thin LAG:Eu (Eu-doped lutetium aluminium garnet, $Lu_3Al_5O_{12}$) scintillator crystal onto the CCD detector with 14 μm pixel size (Koch *et al.*, 1999). The spatial resolution of this detector configuration was around 1 μm, measured with the same model of test pattern mentioned in the previous section.

The tomographic reconstruction was carried out using filtered backprojection with a standard ramp filter (Kak & Slaney, 1988) *via* the *PyHST* software package (Mirone *et al.*, 2010).

An example slice reconstructed without prior phase retrieval or other further processing, showing edge-enhancing X-ray inline phase contrast, is displayed in Fig. 7 (top left). Most of the cellulose fibres are collapsed. This causes the microstructure to be very irregular. The same data set was then reconstructed using projections to which phase retrieval with *ANKAphase* had been applied. The initial parameters for phase retrieval were estimated *via* the CXRO online calculator (Center for X-ray Optics, 2010) and then optimized manually to obtain images that facilitate interpretation and segmentation in an optimal way. A tomographic slice corresponding to the one shown in the top left panel of Fig. 7, but reconstructed after phase retrieval, is depicted in the top right panel of the same figure. Besides the increased contrast
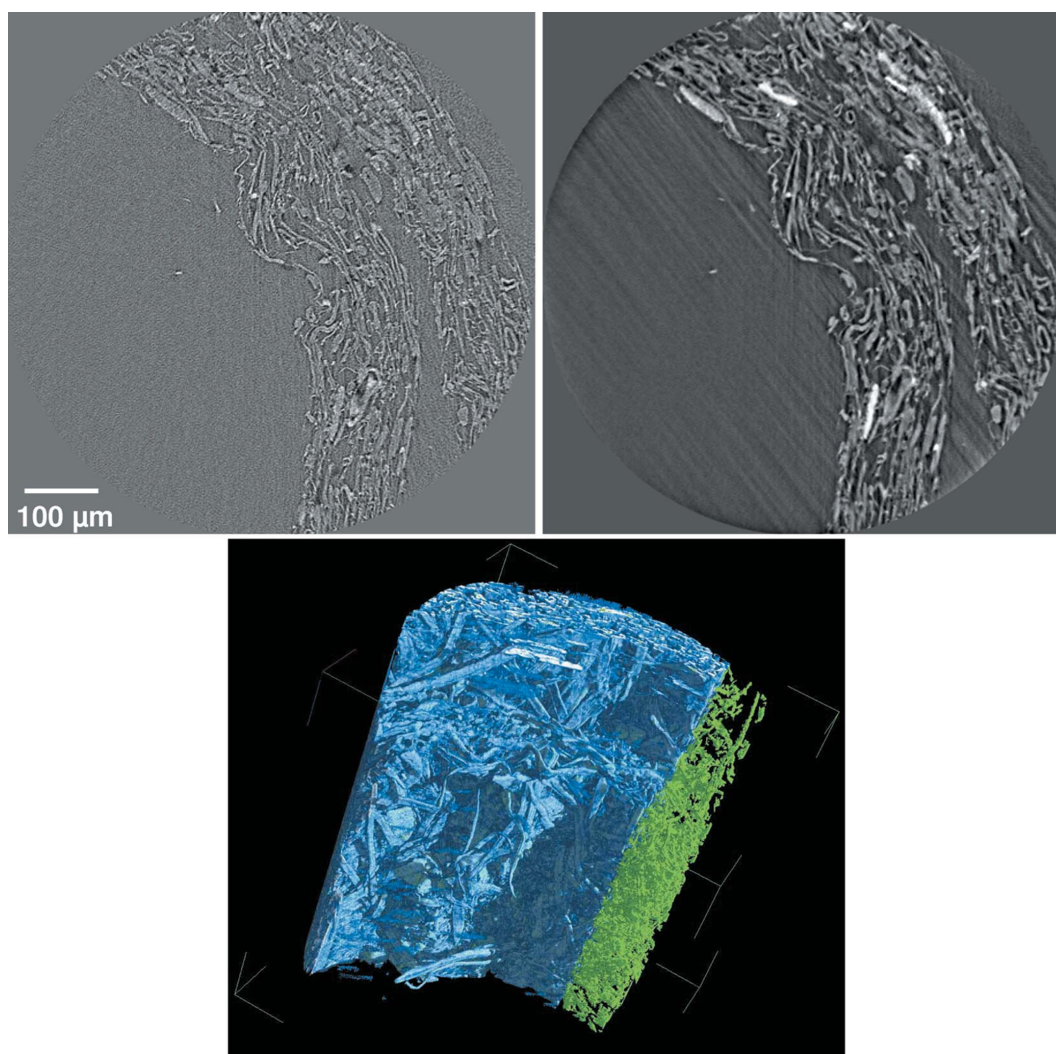

Figure 7
Microstructure of a sample of recycled paper. Top left: standard tomographic reconstruction dominated by X-ray inline phase contrast. It is difficult, if not impossible, to distinguish different materials. Top right: same slice reconstructed from phase-retrieved projections processed by *ANKAphase*. Besides the higher contrast between the sample and the background, different constituents inside the specimen can now be distinguished. Bottom: volume rendering of the segmented tomographic volume data reconstructed from the phase maps. Part of the cellulose constituent (blue–white) is cropped in order to visualize the additives (green).

between the specimen and the background, different additives contained in the paper can now be distinguished. A volume rendering of the segmented tomographic volume reconstructed from the phase-retrieved projections is shown in Fig. 7 (bottom). The multi-constituent data set reveals the additives as well as information on the cellulose fiber structure. For the separation, Boolean volume images were created *via* an algorithm based on region growing in combination with a threshold hysteresis (Rack *et al.*, 2008*a*). Further details about volume analysis tasks that are relevant for this type of data can be found in the literature (Antoine *et al.*, 2002; Ohser *et al.*, 2009).

5.3. Life sciences

The example data shown in this section were acquired as part of a study in which the morphology of different mosquitoes (genus *Anopheles*) had to be compared. It demonstrates that even when polychromatic radiation (here, a filtered white beam from a bending magnet) is used to illuminate the sample, the algorithm used by *ANKAphase* can deliver images of high quality in terms of spatial resolution, contrast and absence of artifacts.

The experiments were carried out at the ANKA light source of the Karlsruhe Institute of Technology (KIT, formerly Forschungszentrum Karlsruhe), Germany, in collaboration with the Entomology Unit and the X-ray Laboratories of the International Atomic Energy Agency (IAEA Laboratories, Seibersdorf, Austria) and the Atominstitut of the Technische Universität Wien (Vienna, Austria). The advantage of phase-sensitive X-ray imaging here is that it allows for probing a sample characterized by very weak or no absorption contrast. This is generally of interest for radiography of soft tissue, small animals and insects, where the available material thickness is not sufficient to produce satisfactory absorption contrast. Another advantage over X ray absorption radiography can be minimization of the radiation dose to the sample. The technique allows the investigation of live animals or the performance of tomographic imaging with longer exposure time and minimum radiation damage to the sensitive and delicate samples (Betz *et al.*, 2007; Socha *et al.*, 2007; Westneat *et al.*, 2008; Rack *et al.*, 2010).

The tomographic scans were performed at the bending-magnet beamline TopoTomo of ANKA (Rack *et al.*, 2009*b*). A white beam from the bending magnet was used, spectrally filtered only by a 0.5 mm-thick beryllium window, a silicon wafer of 1 mm thickness, and approximately 1.5 m of air path. The resulting energy spectrum has its maximum around 20 keV with a bandwidth $\Delta E/E$ of approximately 75%. The image detector consisted of a 25 µm-thick LAG:Eu scintillator, a 4×/NA 0.16 microscope objective and 2.5× eyepiece, and an 'off-the-shelf' CCD-based camera with an array of 4008 × 2672 pixels of size 9 µm (PCO AG, Kelheim, Germany, model pco.4000). The detector thus operated with an effective pixel size of 0.9 µm. A glass filter (type FGL 495, Thorlabs GmbH, Dachau, Germany) was inserted into the optical beam path of the microscope in order to block parasitic lumines-

cence from the scintillator substrate, a 160 µm-thick yttrium aluminium garnet (YAG, $Y_3Al_5O_{12}$) (Rack *et al.*, 2008*b*), which would otherwise have degraded the spatial resolution. The resulting resolution was experimentally determined to be approximately 2.5 µm (Rack *et al.*, 2009*b*).

The sample–detector distance was approximately 50 mm. 1000 projection images of the chemically fixed specimen were taken during rotation over a range of 180°. Here, as in the previous examples, standard filtered backprojection tomographic reconstruction using the software package *PyHST* was employed.

In Fig. 8 (top left) an example radiograph of a mosquito head can be seen, dominated by X-ray inline phase contrast. In the same figure the corresponding tomographic reconstruction of an example slice without phase reconstruction is depicted (bottom left). Various detailed features can be distinguished owing to edge enhancement, but the contrast between foreground and background remains poor. For the phase reconstruction, chitin ($C_8H_{13}NO_5$) with a density of 1.4 g cm^{-3} was assumed to be the dominating material in order to determine β and δ (Neville *et al.*, 1976). In order to obtain phase maps without any remaining edge enhancement, the reconstruction parameter 'X-ray photon energy' was set to 18 keV, which corresponds to the mean energy as seen by the imaging detector. The parameter 'propagation distance' had
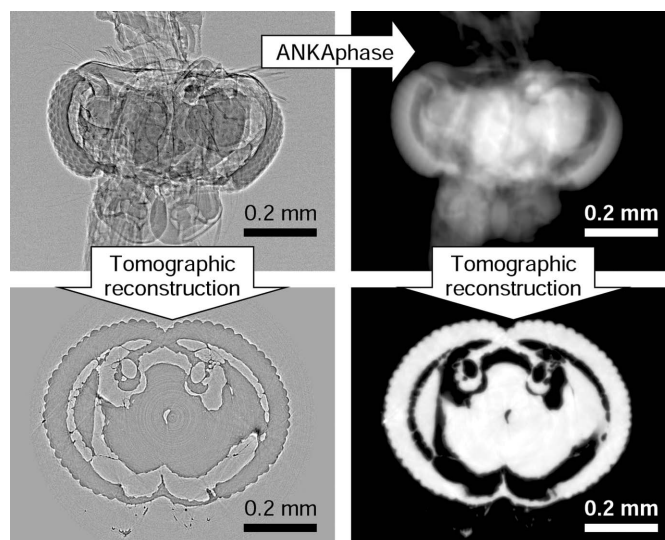

Figure 8
Head of a mosquito, imaged at the ANKA TopoTomo bending-magnet beamline with filtered white-beam radiation. Top left: one of the transmission radiographs recorded in the tomography scan, shown after flat-field normalization. The image is dominated by phase contrast. Edges and interfaces in the object are clearly visible. Bottom left: a slice obtained through direct tomographic reconstruction of the flat-field-corrected transmission radiographs (*i.e.* without phase retrieval) exhibits strong edge contrast, just as the transmission radiograph does. However, the gray values inside the object are so similar to those outside that segmentation is not easily possible. Top right: phase map retrieved from the flat-field-corrected transmission radiograph. The gray values correspond to a map of the projected thickness of the object; lighter tone means greater thickness. Bottom right: tomographic slice obtained from the retrieved phase maps using standard tomographic reconstruction software. A volume rendering based on phase-retrieved tomographic image data is shown in Fig. 9.
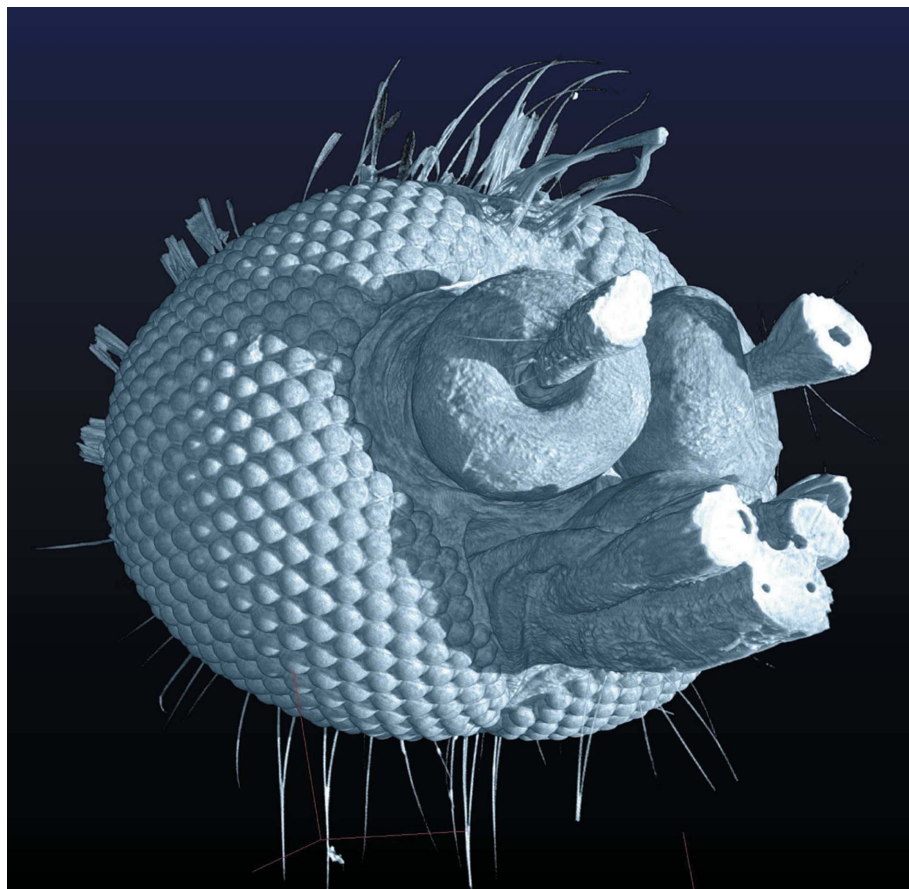
Figure 9
Volume rendering of a phase-retrieved tomographic data set showing the head of a mosquito (genus *Anopheles*), see Fig. 8. Volume data of this kind allow biologists to study morphological differences between individual animals or different species.

(Figs. 8 and 9) have excellent contrast between object and background and uniform reconstructed gray levels inside the object. In particular, they do not show cupping artifacts that would impair segmentation.

The good performance of the algorithm for polychromatic light can also be theoretically explained (Myers *et al.*, 2007).

Through an intuitive graphical user interface, users can plan and launch phase-retrieval processing with no or little training. *ANKAphase* requires, as user input, only the image file paths, the parameters of the experimental set-up (energy, distance, pixel size) and the estimated X-ray optical properties of the sample, δ and β.

The application examples demonstrate the value of *ANKAphase* as a tool that extends the potential of tomography data dominated by X-ray inline phase contrast and acquired at a single propagation distance. It is particularly useful for applications in which data have to be segmented after tomographic reconstruction (*i.e.* the voxels of the reconstructed volume have to be thematically labeled) to enable further volume image analysis. Other typical applications concern cases in which high-quality volume renderings are required to study detailed morphological features in three dimensions.

Users of *ANKAphase* should keep in mind that the algorithm used, like other single-distance phase-retrieval methods, leads to a blurring of the images, as seen, for example, in Fig. 8. Hence, it does not compete with or replace more sophisticated methods such as holotomography (Cloetens *et al.*, 1999), which, on the other hand, need data taken at several different distances between sample and detector. Blurring can be reduced by choosing shorter propagation distances than the experimentally true value when setting the phase-reconstruction parameters. This can somewhat compensate for the finite width of the detector point-spread function (Gureyev *et al.*, 2006); it can also be used to allow some edge enhancing fringes to remain, which will result in a sharper image. This trick comes at the cost that the resulting phase maps no longer have a clearly defined quantitative meaning. Finally, although this may seem trivial, in order to perform quantitative phase reconstructions in three dimensions one has to make sure that the corresponding tomographic reconstruction software used is working in a quantitative manner as well.

ANKAphase can be downloaded from the *ImageJ* plugin web site (National Institutes of Health, 2010a). The distribution includes a user manual in PDF and HTML format.

to be set to 30 mm. The corresponding results can be found in the right-hand panel of Fig. 8. The phase retrieval introduces significant blurring, as can be seen in the radiographic projection. However, the tomographic reconstruction after phase retrieval reveals excellent contrast between foreground and background. Plain thresholding is now sufficient for segmentation; a volume rendering of a complete tomographic data set is shown in Fig. 9. Images of this kind are well suited for studying morphological details of, for example, internal mosquito organs by entomologists.

6. Conclusions

ANKAphase has been designed to give a broader community access to phase retrieval from X-ray inline phase-contrast images. To this end a simple and robust algorithm has been chosen that operates on single radiographs, or on stacks of single-distance images, such as tomography data sets, and allows for non-negligible absorption of X-rays in the sample.

The examples shown demonstrate that, even when polychromatic and moderately coherent synchrotron light is used for illumination, data of high quality can be obtained. Thus, the tomography data acquired with polychromatic X-rays

APPENDIX A
A1. Derivation of equation (8) (boundary treatment)

The main purpose of padding the images is to avoid cross-talk between opposed ends of the projection images, *i.e.* avoid features near the opposite border of the original image showing up in the phase-reconstructed images. Without edge padding, this phenomenon occurs because the convolution of the projection image with a phase-reconstruction kernel is usually carried out in Fourier space, so that the convolution is periodic (Press *et al.*, 2007). The reconstruction kernel includes a backpropagation from the detector plane to the object plane. The (back-) propagation of a point-like feature in the original image, for example a feature located near the edge of the original image, will create a diffraction pattern consisting of a series of concentric bright and dark rings. With increasing distance r from the center of the pattern, the width δ_r of the rings decreases in the same manner as the zone widths of a Fresnel zone plate, *i.e.*

$$\delta_r(r) \simeq \lambda z/(2r). \tag{9}$$

(see Appendix A2).

Note that each of the bright and dark fringes are counted as individual rings; two adjacent bright fringes are thus separated by $2\delta_r$.

Using a detector with given pixel size Δ, the details of the diffraction pattern can no longer be resolved if adjacent bright fringes are spaced by less than the size of a pixel. This also implies that the diffraction pattern of a point-like feature that is further away from the edge of the field of view than a distance r will no longer be resolved at the edge if

$$2\delta_r(r) \lesssim \Delta. \tag{10}$$

By adding a further factor of three (to exclude any remaining aliasing effects) to the requirement expressed in (10) and substituting r from (9) for r_{margin}, we obtain the requirement that the margin width r_{margin} should be at least

$$r_{\mathrm{margin}} \geq 3\lambda z/\Delta. \tag{11}$$

Since the margin width in units of pixels, n_{margin}, a dimensionless quantity, is related to the width r_{margin} (which has the dimension of a length) by $n_{\mathrm{margin}} = r_{\mathrm{margin}}/\Delta$, the equation above is equivalent to (8).

A2. Derivation of equation (9)

As known (Thompson & Vaughan, 2001), the jth ring in a zone-plate pattern has a radius of

$$r_j = \left[j\lambda z + (j\lambda/2)^2 \right]^{1/2} \tag{12}$$

$$\simeq (j\lambda z)^{1/2} \quad \text{for} \quad z \gg j\lambda. \tag{13}$$

The width of the jth zone can be approximated by

$$\delta_{r_j} = r_{j+1} - r_j \tag{14}$$

$$= (j\lambda z)^{1/2} \left[\left(1 + j^{-1}\right)^{1/2} - 1 \right] \tag{15}$$

$$\simeq (j\lambda z)^{1/2}/(2j) \quad \text{(for } j \gg 1) \tag{16}$$

$$= [\lambda z/(4j)]^{1/2} \tag{17}$$

$$\overset{(10)}{=} \lambda z/(2r_j). \tag{18}$$

Note that we assumed $1 \ll j \ll (z/\lambda)$ in this derivation. Substituting (13) for j we see that this assumption is equivalent to $\lambda z \ll r^2 \ll z^2$. In practice, these assumptions will always be fulfilled. This can be seen by substituting r with r_{margin} from (11), which yields $3(\lambda z)^{1/2} \gg \Delta \gg 3\lambda$ as another equivalent expression of the assumption. The first condition $(\lambda z)^{1/2} \gg \Delta$ is fulfilled because, if the pixel size Δ were not much smaller than the first Fresnel zone width $(\lambda z)^{1/2}$, inline phase contrast could not be resolved in the first place. The second condition $\Delta \gg 3\lambda$ is met even more obviously because the pixel size will always be very much larger than the X-ray wavelength.

APPENDIX B
Hardware and software requirements

B1. Platforms and operating systems

With *ANKAphase* being written in Java it should run on any platform and with any operating system for which Java is available, including Microsoft Windows, Mac OS and GNU/Linux systems. However, the program has so far been tested only on Microsoft Windows XP and Vista, SuSE Linux, Ubuntu and Redhat as well as Mac OS Snow Leopard systems.

B2. Software requirements

In order to run *ANKAphase* the Java Runtime Environment (JRE) is required, version 1.6 (*i.e.* Java SE 6) or higher. JRE is available free of charge from Sun Microsystems (Java Consortium, 2010). *ANKAphase* can be used as a plugin for *ImageJ*. Like *ANKAphase*, *ImageJ* is programmed in Java. In order to run *ANKAphase* as an *ImageJ* plugin, an installation of *ImageJ* using JRE 1.6 or higher needs to be available on the system.

If *ANKAphase* is run as a stand-alone application, *ImageJ* does not need to be installed on the computer.

research papers

article. Their comments have substantially helped us to improve the quality of the paper.

References

Antoine, C., Nygård, P., Gregersen, Ø. W., Holmstad, R., Weitkamp, T. & Rau, C. (2002). *Nucl. Instrum. Methods Phys. Res. A*, **490**, 392–402.

Banhart, J. (2008). *Advanced Tomographic Methods in Materials Research and Engineering.* Oxford University Press.

Beltran, M. A., Paganin, D. M., Uesugi, K. & Kitchen, M. J. (2010). *Opt. Express*, **18**, 6423–6436.

Betz, O., Wegst, U., Weide, D., Heethoff, M., Helfen, L., Lee, W. & Cloetens, P. (2007). *J. Microsc.* **227**, 51–71.

Bonse, U. & Busch, F. (1996). *Prog. Biophys. Mol. Biol.* **65**, 133–169.

Boone, M., Witte, Y. D., Dierick, M., den Bulcke, J. V., Vlassenbroeck, J. & Hoorebeke, L. V. (2009). *Nucl. Instrum. Methods Phys. Res. B*, **267**, 1182–1186.

Bremmer, H. (1952). *Physica*, **18**, 469–485.

Bronnikov, A. V. (2002). *J. Opt. Soc. Am. A*, **19**, 472–480.

Brun, F., Mancini, L., Kasae, P., Favretto, S., Dreossi, D. & Tromba, G. (2010). *Nucl. Instrum. Methods Phys. Res. A*, **615**, 326–332.

Center for X-ray Optics (2010). *The Center for X-ray Optics*, http://www-cxro.lbl.gov/.

Cholewa, M., Ping, Y., Ling, N. M., Juan, L. Z., Moser, H. O., Hwu, Y. & Gureyev, T. E. (2007). *Nucl. Instrum. Methods Phys. Res. B*, **260**, 45–48.

Cloetens, P., Barrett, R., Baruchel, J., Guigay, J.-P. & Schlenker, M. (1996). *J. Phys. D*, **29**, 133–146.

Cloetens, P., Ludwig, W., Baruchel, J., van Dyck, D., van Landuyt, J., Guigay, J. P. & Schlenker, M. (1999). *Appl. Phys. Lett.* **75**, 2912–2914.

Denecke, M. A., de Nolf, W., Rack, A., Tucoulou, R., Cloetens, P., Vitova, T., Falkenberg, G., Abolhassani, S. & Kienzler, B. (2011). *Actinide Nanoparticle Research.* Berlin/Heidelberg: Springer. In the press.

Douissard, P.-A., Cecilia, A., Martin, T., Chevalier, V., Couchaud, M., Baumbach, T., Dupré, K., Kühbacher, M. & Rack, A. (2010). *J. Synchrotron Rad.* **17**, 571–583.

ESRF (2009). *XOP 2.3*, http://www.esrf.eu/UsersAndScience/Experiments/TBS/SciSoft/xop2.3.

ESRF (2010). *Implementation of the EDF Data Format in the SAXS Package*, http://www.esrf.eu/UsersAndScience/Experiments/TBS/SciSoft/OurSoftware/SAXS/SaxsHeader.

Graeff, W. & Engelke, K. (1991). In *Handbook on Synchrotron Radiation*, Vol. 4, edited by S. Ebashi, M. Koch and E. Rubenstein, pp. 361–406. Amsterdam: North-Holland.

Groso, A., Abela, R. & Stampanoni, M. (2006*a*). *Opt. Express*, **14**, 8103–8110.

Groso, A., Stampanoni, M., Abela, R., Schneider, P., Linga, S. & Müller, R. (2006*b*). *Appl. Phys. Lett.* **88**, 214104.

Gureyev, T. E., Nesterets, Y. I., Paganin, D. M., Pogany, A. & Wilkins, S. W. (2006). *Opt. Commun.* **259**, 569–580.

Gureyev, T. E., Raven, C., Snigirev, A., Snigireva, I. & Wilkins, S. W. (1999). *J. Phys. D*, **32**, 563–567.

Gureyev, T. E., Stevenson, A. W., Paganin, D. M., Weitkamp, T., Snigirev, A., Snigireva, I. & Wilkins, S. W. (2002). *J. Synchrotron Rad.* **9**, 148–153.

Irvine, S. C., Paganin, D. M., Dubsky, S., Lewis, R. A. & Fouras, A. (2008). *Appl. Phys. Lett.* **93**, 153901.

Java Consortium (2010). *The Java Web Site*, http://www.java.com/.

Kak, A. C. & Slaney, M. (1988). *Principles of Computerized Tomographic Imaging.* New York: IEEE Press.

Koch, A., Peyrin, F., Heurtier, P., Ferrand, B., Chambaz, B., Ludwig, W. & Couchaud, M. (1999). *Proc. SPIE*, **3659**, 170–179.

Koch, A., Raven, C., Spanne, P. & Snigirev, A. (1998). *J. Opt. Soc. Am. A*, **15**, 1940–1951.

Kohn, V. G. (1997). *Phys. Scr.* **56**, 14–19.

Kohn, V. G., Argunova, T. S. & Je, J. H. (2007). *Appl. Phys. Lett.* **91**, 171901.

Kuznetsov, S. (undated). *X-ray Optics Calculator*, http://www.ipmt-hpm.ac.ru/xcalc/xcalc/ref_index.php.

Labiche, J.-C., Mathon, O., Pascarelli, S., Newton, M. A., Ferre, G. G., Curfs, C., Vaughan, G., Homs, A. & Carreiras, D. F. (2007). *Rev. Sci. Instrum.* **78**, 0901301.

Langer, M., Cloetens, P., Guigay, J.-P. & Peyrin, F. (2008). *Med. Phys.* **35**, 4556–4566.

McMorrow, D. & Als-Nielsen, J. (2011). *Elements of Modern X-ray Physics*, 2nd ed. Chichester: Wiley.

Maleki, M. H. & Devaney, A. J. (1994). *Opt. Eng.* **33**, 3243–3253.

Manke, I., Banhart, J., Haibel, A., Rack, A., Zabler, S., Kardjilov, N., Hilger, A., Melzer, A. & Riesemeier, H. (2007). *Appl. Phys. Lett.* **90**, 214102.

Martin, T., Douissard, P.-A., Couchaud, M., Cecilia, A., Baumbach, T., Dupré, K. & Rack, A. (2009). *IEEE Trans. Nucl. Sci.* **56**, 1412–1416.

Martin, T. & Koch, A. (2006). *J. Synchrotron Rad.* **13**, 180–194.

Martín-Herrero, J. & Germain, C. (2007). *Carbon*, **45**, 1242–1253.

Mayo, S. C., Chen, F. & Evans, R. (2010). *J. Struct. Biol.* **171**, 182–188.

Meng, F., Liu, H. & Wu, X. (2007). *Opt. Express*, **15**, 8383–8390.

Mirone, A., Wilcke, R., Hammersley, A. & Ferrero, C. (2010). *PyHST – High Speed Tomographic Reconstruction*, http://www.esrf.eu/UsersAndScience/Experiments/TBS/SciSoft/.

Mochales, C. M., Maerten, A., Rack, A., Cloetens, P., Mueller, W.-D., Zaslansky, P. & Fleck, C. (2011). *Acta Biomater.* Accepted.

Moosmann, J., Hofmann, R., Bronnikov, A. & Baumbach, T. (2010). *Opt. Express*, **18**, 25771–25785.

Myers, G. R., Mayo, S. C., Gureyev, T. E., Paganin, D. M. & Wilkins, S. W. (2007). *Phys. Rev. A*, **76**, 045804.

National Institute of Standards & Technology (2004). NIST Standard Reference Database 126, http://www.nist.gov/pml/data/xraycoef/.

National Institutes of Health (2010*a*). *ImageJ ANKAphase Plugin*, http://rsbweb.nih.gov/ij/plugins/ankaphase/.

National Institutes of Health (2010*b*). *ImageJ*, http://rsb.info.nih.gov/ij/.

Neville, A. C., Parry, D. A. & Woodhead-Galloway, J. (1976). *J. Cell Sci.* **21**, 73–82.

Nugent, K. A., Gureyev, T. E., Cookson, D. F., Paganin, D. & Barnea, Z. (1996). *Phys. Rev. Lett.* **77**, 2961–2964.

Ohser, J., Redenbach, C. & Schladitz, K. (2009). *Image Anal. Stereol.* **28**, 179–185.

Ohser, J. & Schladitz, K. (2009). *3D Images of Materials Structures: Processing and Analysis.* Weinheim/Berlin: Wiley-VCH.

Paganin, D., Mayo, S. C., Gureyev, T. E., Miller, P. R. & Wilkins, S. W. (2002). *J. Microsc.* **206**, 33–40.

Peele, A. G., De Carlo, F., McMahon, P. J., Dhal, B. B. & Nugent, K. A. (2005). *Rev. Sci. Instrum.* **76**, 083707.

Press, W. H., Teukolsky, S. A., Vetterling, W. T. & Flannery, B. P. (2007). *Numerical Recipes: The Art of Scientific Computing*, 3rd ed., ch. 13, pp. 643–644. New York: Cambridge University Press.

Rabaglino, E., Baruchel, J., Boller, E., Elmoutaouakkil, A., Ferrero, C., Ronchi, C. & Wiss, T. (2003). *Nucl. Instrum. Methods Phys. Res. B*, **200**, 352–357.

Rack, A., García-Moreno, F., Schmitt, C., Betz, O., Cecilia, A., Ershov, A., Rack, T., Banhart, J. & Zabler, S. (2010). *J. X-ray Sci. Technol.* **18**, 429–441.

Rack, A., Helfen, L., Baumbach, T., Kirste, S., Banhart, J., Schladitz, K. & Ohser, J. (2008*a*). *J. Microsc.* **232**, 282–292.

Rack, A., Helwig, H.-M., Bütow, A., Rueda, A., Matijasević-Lux, B., Helfen, L., Goebbels, J. & Banhart, J. (2009*a*). *Acta Mater.* **57**, 4809–4821.

Rack, A., Weitkamp, T., Bauer Trabelsi, S., Modregger, P., Cecilia, A., dos Santos Rolo, T., Rack, T., Haas, D., Simon, R., Heldele, R., Schulz, M., Mayzel, B., Danilewsky, A. N., Waterstradt, T., Diete,

W., Riesemeier, H., Müller, B. R. & Baumbach, T. (2009b). *Nucl. Instrum. Methods Phys. Res. B*, **267**, 1978–1988.

Rack, A., Zabler, S., Müller, B. R., Riesemeier, H., Weidemann, G., Lange, A., Goebbels, J., Hentschel, M. & Görner, W. (2008b). *Nucl. Instrum. Methods Phys. Res. A*, **586**, 327–344.

Sanchez del Rio, M. & Dejus, R. J. (1998). *Proc. SPIE*, **3448**, 340–345.

Schelokov, I., Weitkamp, T. & Snigirev, A. (2002). *Opt. Commun.* **213**, 247–258.

Snigirev, A., Snigireva, I., Kohn, V. & Kuznetsov, S. (1995). *Rev. Sci. Instrum.* **66**, 5486–5492.

Socha, J. J. & De Carlo, F. (2008). *Proc. SPIE*, **7078**, 70780A.

Socha, J. J., Westneat, M. W., Harrison, J. F., Waters, J. S. & Lee, W.-K. (2007). *BMC Biol.* **5**, 6.

Stevenson, A. W., Gureyev, T. E., Paganin, D., Wilkins, S. W., Weitkamp, T., Snigirev, A., Rau, C., Snigireva, I., Youn, H. S., Dolbnya, I. P., Yun, W., Lai, B., Garrett, R. F., Cookson, D. J., Hyodo, K. & Ando, M. (2003). *Nucl. Instrum. Methods Phys. Res. B*, **199**, 427–435.

Stiller, M., Rack, A., Zabler, S., Goebbels, J., Dalügge, O., Jonscher, S. & Knabe, C. (2009). *Bone*, **44**, 619–628.

Stock, S. R. (2008). *MicroComputed Tomography: Methodology and Applications.* Boca Raton: CRC Press.

Thompson, A. C. & Vaughan, D. (2001). *X-ray Data Booklet*, 2nd ed. Lawrence Berkeley National Laboratory, University of California, CA, USA (http://xdb.lbl.gov/).

Thurner, P., Müller, B., Beckmann, F., Weitkamp, T., Rau, C., Müller, R., Hubbell, J. A. & Sennhauser, U. (2003). *Nucl. Instrum. Methods Phys. Res. B*, **200**, 397–405.

Tuohimaa, T., Otendal, M. & Hertz, H. M. (2007). *Appl. Phys. Lett.* **91**, 074104.

Wang, Y. J., Im, K.-S., Fezzaa, K., Lee, W. K., Wanga, J., Micheli, P. & Laub, C. (2006). *Appl. Phys. Lett.* **89**, 151913.

Weitkamp, T. (2002). *Imaging and Tomography with High Resolution Using Coherent Hard Synchrotron Radiation.* Göttingen: Cuvillier Verlag.

Weitkamp, T., Raven, C. & Snigirev, A. A. (1999). *Proc. SPIE*, **3772**, 311–317.

Westneat, M. W., Betz, O., Blob, R. W., Fezzaa, K., Cooper, W. J. & Lee, W.-K. (2003). *Science*, **299**, 558–560.

Westneat, M. W., Socha, J. J. & Lee, W.-K. (2008). *Annu. Rev. Physiol.* **70**, 119–142.

Wilkins, S. W., Gureyev, T. E., Gao, D., Pogany, A. & Stevenson, A. W. (1996). *Nature (London)*, **384**, 335–337.

Wu, X., Liu, H. & Yan, A. (2005). *Opt. Lett.* **30**, 379–381.

Wu, X. & Yan, A. (2009). *Opt. Express*, **17**, 11187–11196.

Xu, F., Helfen, L., Moffat, A. J., Johnson, G., Sinclair, I. & Baumbach, T. (2010). *J. Synchrotron Rad.* **17**, 222–226.

Zabler, S., Rueda, A., Rack, A., Riesemeier, H., Zaslansky, P., Manke, I., Garcia-Moreno, F. & Banhart, J. (2007). *Acta Mater.* **55**, 5045–5055.